Transport of spheres suspended in the fluid flowing between hexagonally arranged cylinders

By MASAKO SUGIHARA-SEKI

Faculty of Engineering, Kansai University, Suita, Osaka 564-8680, Japan

The motion of a spherical particle suspended in an incompressible Newtonian fluid flowing longitudinally between hexagonally arranged circular cylinders has been numerically analysed by a finite-element method in the Stokes flow regime. The results are applied to study the diffusive and convective transport of spherical solutes across the vascular endothelial surface glycocalyx, based on the quasi-periodic ultrastructural model. The obtained values of diffusive permeability and reflection coefficient of the solutes show a reasonable agreement with experimental observations, and conform to the hypothesis that the endothelial surface glycocalyx forms the primary size selective structure to solutes in microvascular permeability.

1. Introduction

The luminal surface of vascular endothelial cells is lined with a glycocalyx, a layer of macromolecules such as proteoglycans and glycoproteins. The importance of its physiological functions has been widely recognized, since the glycocalyx has been shown to influence several aspects of vascular function, including endothelial permeability to water and solutes, leukocyte adhesion and emigration, microvascular haematocrit and metabolic products of endothelial cells (Pries, Secomb & Gaehtgens 2000; Weinbaum *et al.* 2003). Among these functions, we focus here on its role as a molecular sieve for the filtering of plasma proteins, when they are transported between the circulating blood and surrounding tissues.

Detailed structures of the glycocalyx were not known until recently. By structural analysis of glycocalyx samples prepared in a variety of ways for electron microscopy, Squire *et al.* (2001) showed that there is an underlying three-dimensional fibrous meshwork within the glycoclayx with characteristic spacings of about 20 nm. Based on this observation, they proposed a structural model of the endothelial surface glycocalyx, as shown in figure 1. It consists of clusters of fibrous strands projecting normally to the surface of the luminal wall and the core protein clusters form a hexagonal two-dimensional lattice on the endothelial cell surface, with an intercluster spacing of about 100 nm. Within each cluster there is a common parallel periodicity of about 20 nm. Squire *et al.* assumed a two-dimensional square lattice of the core proteins with 20 nm spacing in each cluster across the endothelial surface; they pointed out that this spacing and a fibre diameter of 10–12 nm provide just the size regime to account satisfactorily for the observed molecular filtering. Instead of the square lattice of the core proteins, Weinbaum *et al.* (2003) proposed their hexagonal arrangement with a spacing of 20 nm in the idealized model, and showed that this new structure provides a much improved description of the hydraulic resistance of
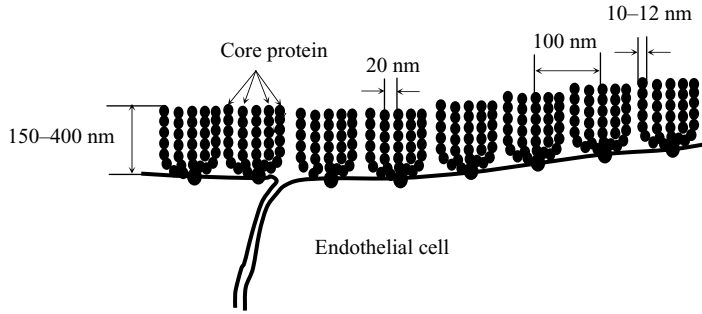
FIGURE 1. Sketch of the glycocalyx bush structure showing core protein arrangement and anchoring foci (modified from Squire *et al.* 2001; Weinbaum *et al.* 2003).

the glycocalyx as well as a better prediction for the reflection coefficient, compared to previous predictions.

Based on a simplified model of the glycocalyx structure proposed by Squire *et al.* (2001) and Weinbaum *et al.* (2003), we here consider transport of solutes and solvent through the glycoclayx, using an idea developed for membrane transport. From thermodynamic principles, the solute flux J_s and solvent flux J_v per unit cross-sectional area of a membrane can be approximately expressed as the summation of two terms proportional to an applied concentration difference Δc of solutes and pressure difference Δp across the membrane (Kedem & Katchalsky 1958, 1961; Curry 1984; Taylor & Granger 1984):

$$J_s = \omega RT \Delta c + (1-\sigma)c^* J_v, \tag{1a}$$

$$J_v = L_p(\Delta p - \sigma RT \Delta c), \tag{1b}$$

where R is the gas constant, T is absolute temperature and c^* is the average concentration of solutes within the passages of the membrane. In these equations, called as Kedem–Katchalsky equations, the transport property is represented by three parameters: the diffusive permeability ω; the hydraulic conductivity L_p; and the reflection coefficient σ. In the present study, we consider the motion of solutes and the suspending fluid between a regular arrangement of core proteins as a model of the glycocalyx, and directly evaluate these coefficients L_p, ω and σ, by numerical computations. In §2.1, we shall derive the expressions for ω and σ in terms of fluid mechanics, and the results and discussion will be provided in §3 on the transport property of the endothelial surface glycocalyx.

2. Formulation and methods

2.1. *Expressions for ω and σ*

We consider the transport properties of the glycocalyx, by using a simple model based on the glycocalyx structure in figure 1. We assume that the solutes are rigid spheres with radius a, the solvent is an incompressible Newtonian fluid with viscosity μ, and the solution is dilute. For simplicity, the core proteins of the glycocalyx in figure 1 are assumed to have a circular cylindrical shape with diameter $2r_f = 12$ nm, and to form a hexagonal arrangement with length $L = 20$ nm, as shown in figure 2. We also assume that the length of the core proteins, l, is long enough compared to a, r_f and L so that the end effects on the motion of the solute and the fluid can be neglected.
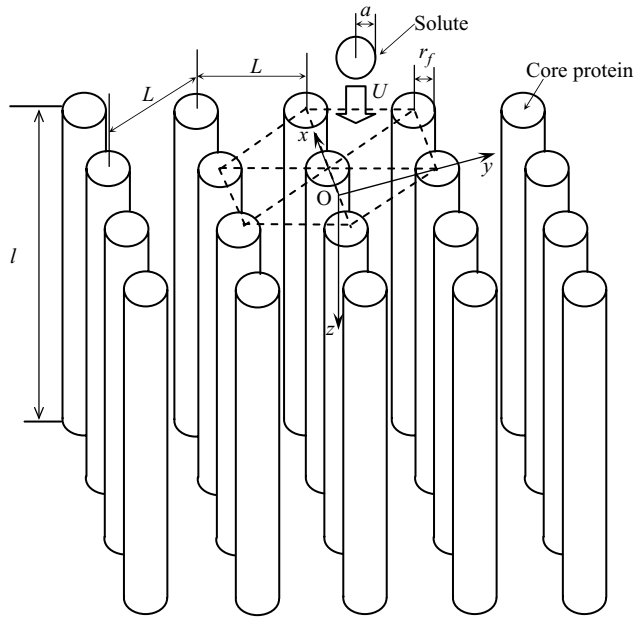
FIGURE 2. Configuration for a solute transport between hexagonally arranged circular cylinders. We consider the case of $a = 2$–$4\,\mathrm{nm}$, $r_f = 6\,\mathrm{nm}$, $L = 20\,\mathrm{nm}$, and $l = 150$–$400\,\mathrm{nm}$.

The effect of inertia on the motion of the solute and the fluid can be neglected, which is a prerequisite condition for equation (1).

We analyse the flow field around a solute placed at various positions in the cross-section of the hexagonally arranged cylinders, and calculate the drag force F acting on the solute exerted by the surrounding fluid and the torque M about its centre, in the three cases of (a) a solute moving parallel to the axis of the cylinders in an otherwise quiescent fluid, (b) the fluid flowing over a stationary solute, driven by a pressure gradient along the cylinder axis, and (c) a solute rotating with a constant angular velocity in an otherwise quiescent fluid. In case (c), the direction of rotation is specified depending on the position of the solute, as will be explained below. Denoting the translational velocity of the solute in case (a) as U, the mean velocity of the fluid averaged over the cross-sectional area available for the fluid in case (b) as V, and the angular velocity of the solute in case (c) as Ω, we define drag coefficients and torque coefficients as $F_t = F/6\pi\mu a U$ and $M_t = M/8\pi\mu a^2 U$ in case (a), $F_0 = F/6\pi\mu a V$ and $M_0 = M/8\pi\mu a^2 V$ in case (b), and $F_r = F/6\pi\mu a^2 \Omega$ and $M_r = M/8\pi\mu a^3 \Omega$ in case (c). In general, the drag forces and torques are vectors with three components. However, linearity of the governing equations and symmetry of the configuration indicate that the drag forces in cases (a) and (b) have only the components along the axis of the cylinders. In addition, we treat only the configurations where the direction of the torque on the solute is known beforehand, that will be explained in the following paragraphs. The direction of rotation in case (c) is determined according to it. As a result, all quantities appeared here can be expressed as scalars.

We consider steady and isothermal transport of the solutes at $T(\mathrm{K})$ along the axis of the cylinders when the pressure difference and the concentration difference of the solutes are present across both ends of the cylinders. Mechanical and thermal equilibrium requires that the hydrodynamic force on a solute exerted by

the surrounding fluid should be balanced with the gradient of the chemical potential of the solutes, and the torque on the solute vanishes. If we assume that the pressure p and the solute concentration c are constant over a cross-section and they vary only along the axis of cylinders, i.e. the z-direction, these conditions yield for a solute with velocity U and angular velocity Ω immersed in a mean flow V (Sugihara-Seki 2004),

$$\frac{RT}{N}\frac{dc}{c\,dz} + v_s\frac{dp}{dz} = 6\pi\mu a(UF_t + a\Omega F_r + VF_0), \qquad (2a)$$

$$8\pi\mu a^2(UM_t + a\Omega M_r + VM_0) = 0, \qquad (2b)$$

where v_s is the volume of the solute $(=(4/3)\pi a^3)$ and N is Avogadro's number. Eliminating the angular velocity, we have

$$cU = -\frac{RT}{6\pi\mu aN}\frac{dc}{dz}\frac{1}{F^*} + cV\frac{G^*}{F^*} - \frac{2a^2}{9\mu}c\frac{dp}{dz}\frac{1}{F^*}, \qquad (3)$$

where

$$F^* = \frac{F_r M_t - M_r F_t}{M_r}, \quad G^* = \frac{M_r F_0 - F_r M_0}{M_r}. \qquad (4a,b)$$

Note that a force-free and torque-free spherical solute placed at any position in the cross-section translates parallel to the axis of the cylinders, as evident from symmetry considerations, so that there are no preferred positions of the solute in the cross-section. Thus, we assume as a first approximation that all possible positions of the solute in the cross-section have equal probability, except for steric exclusion near the cylinder surfaces. As a next step, we need to modify this assumption, considering some possible interactions between the solute and the glycocalyx such as electrostatic forces on their surface charges. In the present study, however, we focus on the fluid mechanical interaction and do not consider the charge effect, since it was shown experimentally that molecular size is a more significant determinant of solute permeability in continuous capillaries than solute charge (Adamson, Huxley & Curry 1988).

Under the equal probability assumption, we have an expression for the solute flux as $J_s = (1/A)\int_{A^*} cU\,dA$, where A represents the cross-sectional area and A^* is the area available for the centre of the solute, both of which will be specified below. Substituting equation (3) and integrating along the z-axis across both ends of the cylinders with length l yields

$$J_s = \frac{RT}{6\pi\mu aNl}\frac{\Delta c}{A}\int_{A^*}\frac{1}{F^*}\,dA + \frac{c^*V}{A}\int_{A^*}\frac{G^*}{F^*}\,dA - \frac{2a^2}{9\mu}\frac{B}{A}\int_{A^*}\frac{1}{F^*}\,dA, \qquad (5)$$

where

$$c^* = \frac{1}{l}\int_0^l c\,dz, \quad B = \frac{1}{l}\int_0^l c\frac{dp}{dz}\,dz. \qquad (6a,b)$$

The first term on the right-hand side of equation (5) represents the diffusive transport of the solutes due to the concentration difference, and the second term describes the component due to the convection. The third term denotes the diffusive transport due to the pressure gradient. Since the solution is dilute, the coefficient B may be approximately rewritten in terms of the mean concentration c^* and the Darcy permeability K, defined as $J_v = (K/\mu)(\Delta p/l)$, in such a way that $B \approx -c^*(\Delta p/l) \approx -c^*\mu J_v/K$. Then, a comparison with equation (1a) leads to approximate expressions
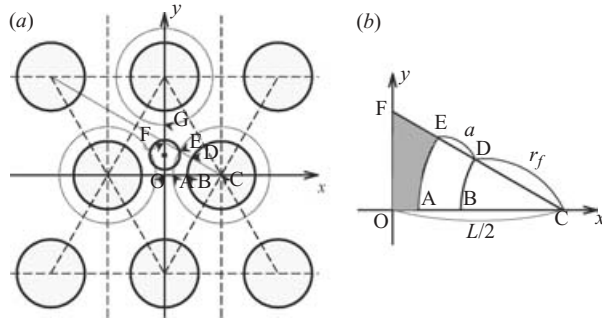
FIGURE 3. Cross-section of the hexagonal arrangement of circular cylinders.

for the diffusive permeability ω and the reflection coefficient σ:

$$\frac{\omega}{\omega_0} = \frac{1}{A} \int_{A^*} \frac{1}{F^*} \, \mathrm{d}A, \tag{7}$$

$$1 - \sigma = \sigma_c + \sigma_d, \quad \sigma_c = \frac{1}{A'} \int_{A^*} \frac{G^*}{F^*} \, \mathrm{d}A, \quad \sigma_d = \frac{2a^2}{9K} \frac{1}{A} \int_{A^*} \frac{1}{F^*} \, \mathrm{d}A. \tag{8a-c}$$

Here, ω_0 is the unrestricted permeability in an unbounded region $(= 1/6\pi\mu a N l)$, and A' is the cross-sectional area available for the fluid. Noting that the mean velocity V of the fluid is defined as the fluid velocity averaged over the region A', not A, we have used the relationship that $J_v = A'V/A$.

2.2. *Method of evaluating* L_p, ω *and* σ

We evaluate the values of ω and σ from equations (7) and (8). Since the whole cross-section can be divided into equal triangular regions such as OCF shown in figure 3, we confine ourselves to this region in a way that A in equations (7) and (8) is the area of triangle OCF, A' is the area of region OBDF which represents the area available for the fluid, and A^* is the area of region OAEF, available for the centre of the solute. Explicitly, $A = L^2/8\sqrt{3}$, $A' = L^2/8\sqrt{3} - \pi r_f^2/12$ and $A^* = L^2/8\sqrt{3} - \pi(r_f + a)^2/12$.

In equations (7) and (8), the integrations should be performed over the hatched region OAEF in figure 3, or A^*. Then, the knowledge of F^* and G^* defined by equation (4) is necessary for all cases when the solute centre is placed at any position in the region of OAEF. In the present study, however, for simplicity of numerical computation, we treat only the cases when the solute centre is located on the perimeter of the region OAEF, that consists of lines OF, FE, OA and arc AE. On the arc AE, $1/F^*$ and G^*/F^* vanish where the solute would touch the surface of cylinders. Since the configurations on the line FE are identical to those on the line FG in figure 3(a), we consider here the configurations where the solute centre is placed on the lines OG and OA. This limitation reduces our numerical computations considerably, since the directions of torque on the solute in cases (a) and (b) can be specified beforehand, i.e. along the x-axis on the line OG and along the y-axis on the line OA. Thus, in case (c), the solute rotation can be confined to be in the x-direction and the y-direction, respectively. In addition, this simplification allows us to halve the computational region, owing to symmetry of the flow geometry, and thus greatly reduce the computational time.

When the solute centre is located on the line OG, it is expressed as $(x, y) = (0, c_y)$, and on the line OA, it is expressed as $(x, y) = (c_x, 0)$, where $0 \leqslant c_y < \sqrt{3}L/2 - r_f - a$

and $0 \leqslant c_x < L/2 - r_f - a$. For a solute with radius a placed at $(0, c_y)$ or $(c_x, 0)$, the flow fields around it were computed for the three cases of (a)–(c), by a finite-element method applied to the Stokes equation and continuity equation (Sugihara-Seki 1996). On the surfaces of the cylinders and the solute, a no-slip boundary condition was adopted. Far upstream and downstream from the solute, the velocity profile was prescribed as that in the absence of the solute, which was obtained by a numerical computation. In the x- and y-directions, periodic boundary conditions were adopted at $x = \pm L/2$ and $y = \pm \sqrt{3}L/2$.

The computational domain was divided into a number of finite elements. Each element has a hexahedral shape with 27 nodes including eight corner nodes (Sugihara-Seki 1996). Using the values of the velocity at the 27 nodes and the values of the pressure at the eight corner nodes, the velocity and pressure within each element were approximated by quadratic and linear functions in terms of local coordinates, respectively. A representative mesh had about 1350 elements and 31 000 unknowns. A finite-element scheme was formulated in terms of the primitive variables based on the variational principle, and the assessment of the numerical error has been done previously (Sugihara-Seki 1996, 2004). Actually, the drag forces acting on a sphere translating in a two-dimensional channel filled with a Newtonian fluid showed an agreement within 2 % between the present analysis and Feng, Ganatos & Weinbaum (1998). We also confirmed the relationship between the drag coefficient on a rotating sphere F_r and the torque coefficient on a translating sphere M_t as $F_r/M_t = 4/3$ with less than 1 % error for all ranges of a, c_x and c_y we examined.

In each case (a), (b) and (c), we have calculated the drag force and torque acting on the solute exerted by the fluid flow. By using the values of $1/F^*$ and G^*/F^* for various positions of the solute centre at lines OA and OG, or the perimeter of the region OAEF, the integrations of equations (7) and (8) were performed approximately by a numerical library SSLII based on Aitken-Lagrange interpolation (Fujitsu manual, FACOM FORTRAN SSLII 99SP). As will be explained in §3.1, the error due to this interpolation is estimated to be at most a few per cent.

As mentioned above, the velocity profile far upstream and downstream from the solute has also been computed, by considering the axial flow of the fluid in the absence of the solute. The results are compared with the analytical solution obtained previously (Sparrow & Loeffler 1959) and found to show a good agreement. Under the condition that the solution is dilute, the integration of this velocity profile over the region A' provides the flow rate of the solution and its division by the area A gives the flux J_v. Then, we can evaluate the hydraulic conductivity L_p as the ratio of J_v and the pressure difference Δp between both ends of the cylinders, or the Darcy permeability K as $J_v \mu l / \Delta p$.

According to the experimental observation of the microvascular endothelial surface glycocalyx of the frog mesentery (Squire *et al.* 2001), we have adopted typical values of the parameters such as $r_f = 6$ nm, $L = 20$ nm, $l = 150 - 400$ nm, and $a = 2 - 4$ nm.

3. Results and discussion

3.1. *Coefficients $1/F^*$ and G^*/F^**

When a solute with radius a ($2 \leqslant a \leqslant 4$ nm) is placed at $(x, y) = (0, c_y)$ or $(c_x, 0)$, the flow field around the solute and the values of the drag coefficients and torque coefficients were computed in cases (a)–(c). Our results showed that $O(F_t) = O(F_0) = O(M_r) = 1$, while $O(M_0) \leqslant 10^{-1}$ and $O(M_t) = O(F_r) \leqslant 10^{-2}$ in all the range we
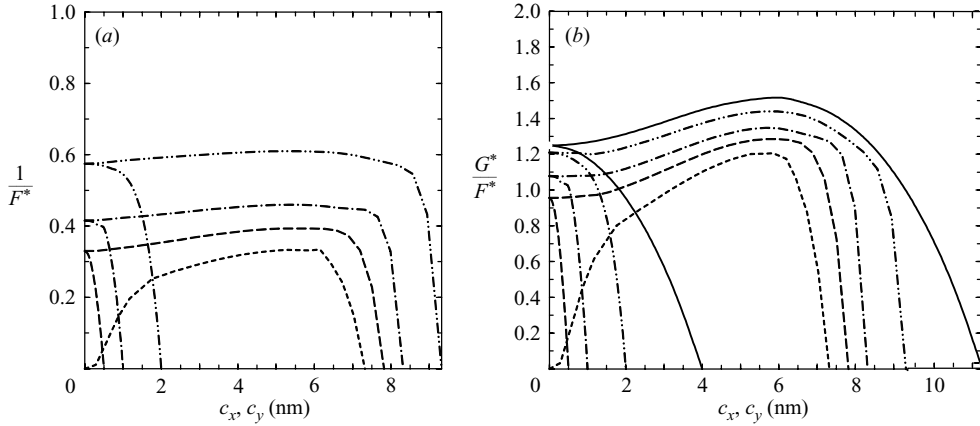
FIGURE 4. (a) Plot of $1/F^*$ for $a = 2$ nm (dash-double dotted curve), 3 nm (dash-dotted curve), 3.5 nm (dashed curve) and 4 nm (dotted curve). (b) Plot of G^*/F^* for $a = 2$ nm (dash-double dotted curve), 3 nm (dash-dotted curve), 3.5 nm (dashed curve) and 4 nm (dotted curve). The solid curve represents the case of $a = 0$, or the velocity profile of the fluid along the x-axis or the y-axis, in the absence of the solute.

considered. Thus, we have

$$1/F^* \approx -1/F_t, \quad G^*/F^* \approx -F_0/F_t. \tag{9a,b}$$

We calculated both sides of equations (9a) and (9b) and found that differences between them are within 10^{-4} and 10^{-3}, for equations (9a) and (9b), respectively. These approximate expressions indicate that the effect of rotational motion of the solute is minor on the solute transport considered here. This property was also pointed out in our previous study for transport of spherical solutes through a circular cylindrical pore (Sugihara-Seki 2004). If we compare the two studies, we see that the solute rotation is even less important in the present case, which may result from the presence of smaller portions of solid boundaries of the flow region; in a circular cylindrical pore, the whole flow region is surrounded by the pore wall where the fluid velocity has to vanish. In fact, the velocity profile of the fluid in the present geometry shows more moderate slopes compared to a Poiseuille flow, when the flow is driven by a pressure gradient along the cylinder axis (see figure 5). It is interesting to note that the quantity represented by equation (9a) corresponds to the mobility in Einstein relation, and equation (9b) represents the translational velocity of a solute relative to the mean velocity of the fluid, U/V, when it is freely suspended in a fluid flow in the absence of the concentration difference of the solutes.

Figures 4(a) and 4(b) show the plots of $1/F^*$ and G^*/F^* as functions of the position of the solute centre, c_x, c_y, for $a = 2$, 3, 3.5 and 4 nm. From linearity of the problem, we will find the same curves if the abscissa is replaced by the dimensionless quantities such as c_x/L and c_y/L for $a/L = 0.1$, 0.15, 0.175 and 0.2. It is evident from figure 4(a) that, for constant a, the values of $1/F^*$ are almost constant over the ranges of c_y except in the proximity of the cylinder surface, and their curves have steep gradients there. Noticing that the ordinate of figure 4(b) represents the translational velocity of a freely floating solute, U/V, we see from figure 4(b) that the freely floating solute translates with a velocity larger than the mean bulk velocity in a wide range of c_y, especially for small solutes, and their velocities steeply decrease to 0 near the cylinder surface.
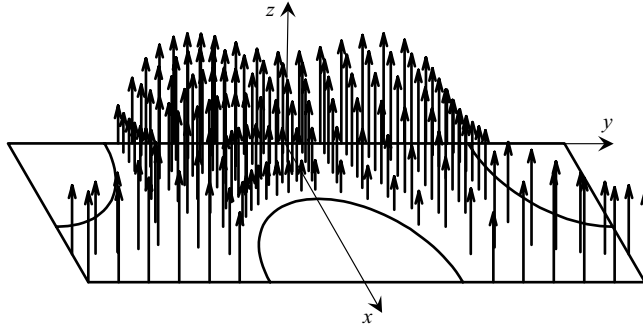
FIGURE 5. Velocity distribution of the fluid in the absence of the solute, in the rectangular region of the cross-section, $0 \leqslant x \leqslant L/2$ and $-\sqrt{3}L/2 \leqslant y \leqslant \sqrt{3}L/2$.

In figure 4(*b*), we also plot the velocity profile of the fluid without the solute, corresponding to the case of $a = 0$, for reference. This profile has been used to estimate the accuracy of the present method of integration in equations (7) and (8). Only from the information of the fluid velocity on the x- and y-axes as shown in figure 4(*b*) or on the perimeter of the region OBDF in figure 3, we have estimated the flow rate over the cross-section OBDF, by the method applied to the integrations in equations (7) and (8). The difference between this obtained value and the exact flow rate is about 2.3 %. Then, the error in the estimation of equation (8*b*) due to the interpolation may be of the order of several per cent. The errors in equations (7) and (8*c*) are expected to be even less since the curves $1/F^*$ in figure 4(*a*) have wider ranges of flat portions compared to those of G^*/F^* in figure 4(*b*).

3.2. *Hydraulic conductivity L_p*

From equation (1*b*), we have

$$L_p = J_v/\Delta p \mid_{\Delta c=0}. \tag{10}$$

This expression indicates that the hydraulic conductivity can be evaluated by the ratio of the fluid flux and the pressure drop across both ends of the cylinders, when the difference in concentration of the solutes is absent. The simplest case satisfying this condition is when there are no solutes and only the fluid is present. As noted above, we have computed the flow velocity numerically in this case, and compared our results with the previous results (Sparrow & Loeffler 1959; Larson & Higdon 1986).

The velocity profile of the fluid is plotted in figure 5, in the rectangular region of $0 \leqslant x \leqslant L/2$ and $-\sqrt{3}L/2 \leqslant y \leqslant \sqrt{3}L/2$. This is comparable to figure 5 of Larson & Higdon (1986). Sparrow & Loeffler (1959) calculated the values of $4\Delta p A'/\mu\theta_0 Vl$, where $\theta_0 = \angle \text{OCF} = \pi/6$, representing the friction factor multiplied by the Reynolds number. From figure 7 of their paper, its value is found to be about 16.3, for the present case of $A'/A = 0.6735$. The corresponding result of our numerical computation is 16.4, showing a good agreement. From the relationship $K = J_v \mu l/\Delta p$, we have

$$K/L^2 = (4A'^2/\theta_0 AL^2)(1/16.4) = 0.0152, \tag{11}$$

where we have used $J_v = VA'/A$. Then, we have the hydraulic conductivity

$$L_p = 0.0152x(L^2/\mu l) = (1.52 - 4.06) \times 10^{-8}\,\text{m}\,\text{Pa}^{-1}\,\text{s}^{-1} \tag{12}$$

for $L = 20\,\text{nm}$, $\mu = 10^{-3}\,\text{Pa}\,\text{s}$ and $l = 150 - 400\,\text{nm}$.
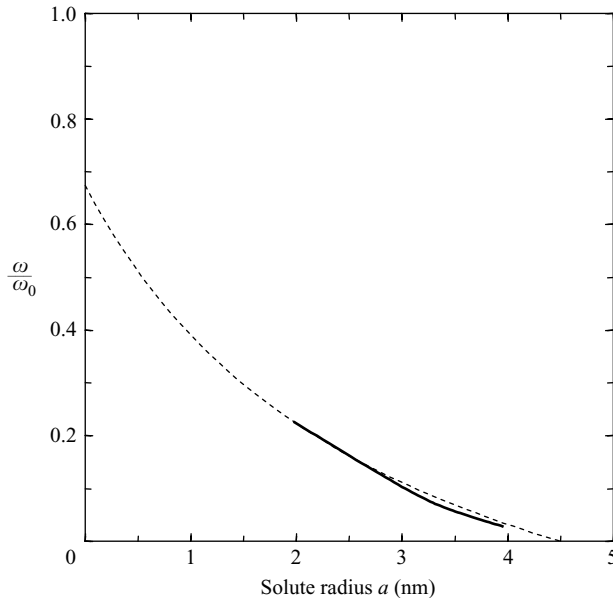
FIGURE 6. The diffusive permeability normalized by the unrestricted permeability. The dashed curve represents the result of the Brinkman medium approach $(\omega/\omega_0)^B$ with $K = 6.10 \, \text{nm}^2$

The contribution of the endothelial glycocalyx to the hydraulic conductivity of the capillary wall was experimentally studied by Adamson (1990), who measured normal capillary hydraulic conductivity of single capillaries of frog mesentery as well as after partial degradation of the endothelial glycocalyx. He observed that the hydraulic conductivity L_p increased from $2.0 \times 10^{-7} \, \text{cm s}^{-1} \, (\text{cmH}_2\text{O})^{-1}$ to $4.9 \times 10^{-7} \, \text{cm s}^{-1}$ $(\text{cmH}_2\text{O})^{-1}$ after enzymatic degradation, a nearly 2.5 fold increase. This result indicates that L_p of the glycocalyx alone is of the order of $10^{-7} \, \text{cm s}^{-1} \, (\text{cm H}_2\text{O})^{-1} \approx 10^{-11} \, \text{m Pa}^{-1} \, \text{s}^{-1}$, which is three orders of magnitude lower than the value of equation (12).

This difference may be attributed to several causes. One of them is that in continuous endothelium, the capillary filtration occurs through interendothelial clefts, whose area is estimated to be about $1/1000$ of the endothelial surface for vessels in frog mesentery (Fu *et al.* 1994). So, if the fluid flows only perpendicularly to the endothelial surface through the glycocalyx, and then into the clefts, the hydraulic conductivity of the glycocalyx should be given by the value of equation (12) multiplied by the area ratio of the cleft entrance relative to the endothelial surface (10^{-3}). Another cause may be that the water inside the glycocalyx is not an ordinary fluid, but in a gel-like state, so that the value of the fluid viscosity may be enhanced. In addition, the presence of a three-dimensional fibrous mesh network between core proteins may make the fluid flow more like a Brinkman type flow than a Newtonian flow (see the next section), which apparently increases the Darcy permeability K of the whole glycocalyx. More detailed studies are necessary to clarify the relationship between the present result and experimental measurements.

3.3. *Diffusive permeability* ω

By performing the integration of equation (7), we have calculated the diffusive permeability as a function of the solute radius a. Figure 6 represents our results, together with the curve obtained based on the Brinkman medium approximation.

The Brinkman medium is a continuum material characterized by a Newtonian viscosity μ and the Darcy permeability K, in such a way that its velocity $\boldsymbol{u}$ is governed by the equation:

$$-\nabla p + \mu \nabla^2 \boldsymbol{u} - \frac{\mu}{K} \boldsymbol{u} = 0. \tag{13}$$

The Brinkman medium has been widely used to represent approximately the viscous flow through porous media or fibrous media, under the idea that the effect of the presence of solid materials on the flow is approximated by that of continuously distributed point forces whose magnitude is proportional to the flow velocity (Darcy's law). Adopting this approximation in the present problem, we assume the glycocalyx as a continuum material, with the Darcy permeability K given by equation (11). Since a spherical particle translating in an otherwise quiescent Brinkman medium experiences the drag force (Brinkman 1947; Sugihara-Seki 2004):

$$-F_t = 1 + a/\sqrt{K} + (1/9)(a^2/K), \tag{14}$$

equation (7) together with equation (9a) provides

$$\left(\frac{\omega}{\omega_0}\right)^B \approx \frac{A^*}{A} \frac{1}{1 + a/\sqrt{K} + (1/9)(a^2/K)}. \tag{15}$$

This equation is plotted as a dashed curve in figure 6 when $K = 0.0152 \times L^2 = 6.10\,\text{nm}^2$ (equation (11)). A fairly good agreement of our obtained values with this curve indicates that the Brinkman medium approximation provides reasonable prediction for the diffusive permeability of the solutes, if the Darcy permeability is properly given.

Figure 6 shows that the diffusive permeability normalized by the unrestricted value decreases with increasing solute radius. In experiments, this decline with molecular size has been known for a long time as 'restricted diffusion' (Pappenheimer, Renkin & Borrero 1951). The measurements of restricted diffusion of hydrophilic solutes at walls of microvessels in skeletal muscle showed that it falls by more than an order of magnitude as molecular radius increases from 0.23 to 3.6 nm (Michel & Curry 1999). This tendency seems in accord with our results shown in figure 6. Since similar relations between the normalized diffusive permeability and molecular size were found in other types of microvessel, it is suggested that the detailed structure of the endothelial surface glycocalyx plays an important role in the size selective properties of the solute diffusion.

3.4. *Reflection coefficient σ*

Integrations of equations (8b) and (8c) give the values of σ_c and σ_d. These results as well as σ are plotted in figure 7. The steric condition results in $\sigma = 1$ at $a = L/\sqrt{3} - r_f$, or $a = 5.55\,\text{nm}$ for $L = 20\,\text{nm}$ and $r_f = 6\,\text{nm}$. This is shown as an asterisk in figure 7(a).

From equations (7) and (8c), we have

$$\sigma_d = \frac{2a^2}{9K}\left(\frac{\omega}{\omega_0}\right). \tag{16}$$

The dashed curve σ'_d in figure 7(b) represents equation (16) when equation (15) is substituted as (ω/ω_0) with $K = 6.10\,\text{nm}^2$. Apparently, $G^*/F^* \approx -F_0/F_t \approx 1$ for small a. In this case, we have from equation (8b) that $\sigma_c \approx A^*/A'$. This is also plotted in figure 7(b) as a dotted curve σ'_c.
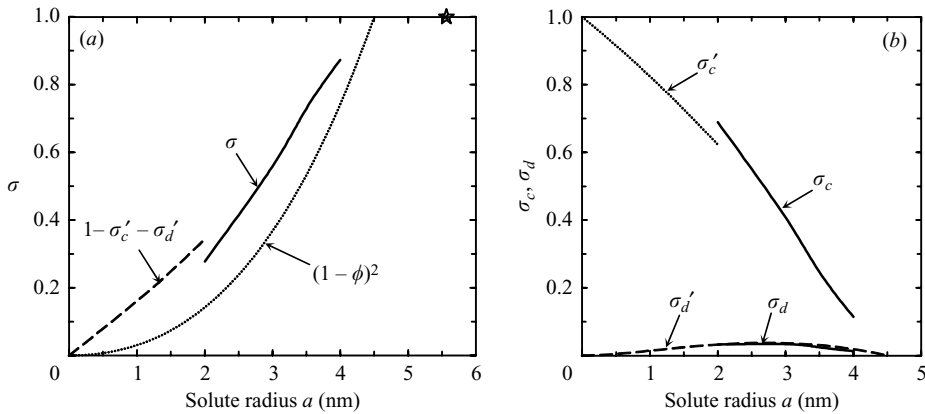
FIGURE 7. (*a*) The reflection coefficient σ and (*b*) σ_c and σ_d. The solid curves represent the present results. (*b*), The dotted curve represents $\sigma_c' = A^*/A'$, and the dashed curve shows $\sigma_d' = (2a^2/9K)(\omega/\omega_0)^B$ with equations (11) and (15).

The curve for σ when the above approximate expressions are adopted for σ_c and σ_d is plotted as a dashed curve in figure 7(*a*). Conventionally, the reflection coefficient is expressed in terms of the solute partition coefficient $\phi = A^*/A'$ as

$$\sigma = (1 - \phi)^2. \tag{17}$$

This expression was originally derived by Ferry (1936) for the solute transport in a circular cylindrical pore, under the assumption that a solute in the pore moves at the undisturbed local velocity of the solvent, i.e. a Poiseuille flow. Equation (17) is also plotted in figure 7(*a*) as a dotted curve. A comparison of equation (17) and our results indicates that the conventional method (equation (17)) generally underestimates the reflection coefficient. This tendency is in accord with that for a spherical solute in a cylindrical pore (Sugihara-Seki 2004), and is understood from the fact that equation (17) does not account for the retardation of a floating solute owing to the fluid mechanical interaction between the solute and the boundary walls.

Experiments have shown that, although the absolute values of L_p and ω to macromolecules vary by several orders of magnitude depending on types of microvessels, the microvessels in very different tissues have similar values for σ (Michel & Curry 1999). It has been found that the σ values to serum albumin ($a = 3.6$ nm) are nearly equal to 0.8 in many different microvascular beds, including cat hindlimb, rat hindlimb, dog heart, frog mesentery, rabbit salivary gland and dog small intestine. The present result shown in figure 7 explains these measurements much better than previous analyses. This agreement may support the idea that the reflection coefficient is largely determined by the luminal glycocalyx (Curry & Michel 1980; Hu & Weinbaum 1999).

4. Conclusions

The endothelial cells of microvessels form the critical barrier controlling the material exchange between circulating blood and body tissues. In order to assess the contribution of the endothelial surface glycocalyx as a molecular sieve for the filtering of plasma proteins, we have considered the transport of spherical solutes

suspended in the fluid flowing between hexagonally arranged cylinders, based on the quasi-periodic ultrastructural model for the glycocalyx proposed in Squire *et al.* (2001). By analysing numerically the Stokes flow around a spherical solute, we have directly evaluated the transport property of the glycocalyx. The obtained values of the solute diffusive permeability and reflection coefficient show reasonable agreement with experimental observations, and suggest that the endothelial surface glycocalyx forms the primary size selective structure to solutes in microvascular permeability.

The present study is our first approach to understanding physiological functions of the endothelial surface glycocalyx. We focus here on the effect of its geometry on the transport property. To arrive at a more comprehensive understanding, further studies are necessary, including considerations of its surfaces charges, gel-like state of the fluid inside, detailed structures existing between core proteins, and so on.

REFERENCES

ADAMSON, R. H. 1990 Permeability of frog mesenteric capillaries after partial pronase digestion of the endothelial gylcocalyx. *J. Physiol.* **428**, 1–13.

ADAMSON, R. H., HUXLEY, V. H. & CURRY, F. E. 1988 Single capillary permeability to proteins having similar size but different charge. *Am. J. Physiol.* **254**, H304–H312.

BRINKMAN, H. C. 1947 A calculation of the viscous force exerted by a flowing fluid in a dense swarm of particles. *Appl. Sci. Res.* A **1**, 27–34.

CURRY, F. E. 1984 Mechanics and thermodynamics of transcapillary exchange. In *Handbook of Physiology*, vol. 4, part 1, pp. 309–374.

CURRY, F. E. & MICHEL, C. C. 1980 A fiber matrix model of capillary permeability. *Microvasc. Res.* **20**, 96–99.

FENG, J., GANATOS, P. & WEINBAUM, S. 1998 Motion of a sphere near planar confining boundaries in a Brinkman medium. *J. Fluid Mech.* **375**, 265–296.

FERRY, J. D. 1936 Statistical evaluation of sieve constants in ultrafiltration. *J. Gen. Physiol.* **20**, 95–104.

FU, B. M., WEINBAUM, S., TSAY, R. Y. & CURRY, F. E. 1994 A junction-orifice-fiber entrance layer model for capillary permeability: application to frog mesenteric capillaries. *J. Biomech. Engng* **116**, 502–513.

HU, X. & WEINBAUM, S. 1999 A new view of Starling's hypothesis at the microstructural level. *Microvasc. Res.* **58**, 281–304.

KEDEM, O. & KATCHALSKY, A. 1958 Thermodynamic analysis of the permeability of biological membranes to non-electrolytes. *Biochim. Biophys. Acta* **27**, 229–246.

KEDEM, O. & KATCHALSKY, A. 1961 A physical interpretation of the phenomenological coefficients of membrane permeability. *J. Gen. Physiol.* **45**, 143–179.

LARSON, R. E. & HIGDON, J. J. L. 1986 Microscopic flow near the surface of two-dimensional porous media. Part 1. Axial flow. *J. Fluid Mech.* **166**, 449–472.

MICHEL, C. C. & CURRY, F. E. 1999 Microvascular permeability. *Physiol. Rev.* **79**, 703–761.

PAPPENHEIMER, J. R., RENKIN, E. M. & BORRERO, J. M. 1951 Filtration, diffusion and molecular sieving through peripheral capillary membranes. A contribution to the pore theory of capillary permeability. *Am. J. Phyisol.* **167**, 13–46.

PRIES, A. R., SECOMB, T. W. & GAEHTGENS, P. 2000 The endothelial surface layer. Pflügers Archiv: *Eur. J. Physiol.* **440**, 653–666.

SPARROW, E. M. & LOEFFLER, JR A. L. 1959 Longitudinal laminar flow between cylinders arranged in regular array. *AIChE J.* **5**, 325–330.

SUGIHARA-SEKI, M. 1996 The motion of an ellipsoid in tube flow at low Reynolds numbers. *J. Fluid Mech.* **324**, 287–308.

SUGIHARA-SEKI, M. 2004 Motion of a sphere in a cylindrical tube filled with a Brinkman medium. *Fluid Dyn. Res.* **34**, 59–76.

SQUIRE, J. M., CHEW, M., NNEJI, G., NEAL, C., BARRY, J. & MICHEL, C. 2001 Quasi-periodic substructure in the microvessel endothelial glycocalyx: a possible explanation for molecular filtering? *J. Struct. Biol.* **136**, 239–255.

TAYLOR, A. E. & GRANGER, D. N. 1984 Exchange of macromolecules across the microcirculation. In *Handbook of Physiology*, vol. 4, part 1, pp. 467–520.

WEINBAUM, S., ZHANG, X., HAN, Y., VINK, H. & COWIN, S. C. 2003 Mechanotransduction and flow across the endothelial glycocalyx. *PNAS* **100**, 7988–7995.